Inorganic Chemistry

pubs.acs.org/IC

Article

# Emission Enhancement and Energy Transfers in $YV_{0.5}P_{0.5}O_4$ Nanoparticles Codoped with $Eu^{3+}$ and $Bi^{3+}$ Ions

Marta Wujczyk,* Sara Targonska, Philippe Boutinaud, John M. Reeks, Adam Watras, and Rafal J. Wiglusz*

Cite This: *Inorg. Chem.* 2022, 61, 12237−12248

Read Online

ACCESS | Metrics & More | Article Recommendations

**ABSTRACT:** In this study, solid-state solutions of yttrium orthovanadate-phosphate with varying concentrations of codopants ($Eu^{3+}$, $Bi^{3+}$) have been obtained via coprecipitation. An ionic radii mismatch between $V^{5+}$ and $P^{5+}$ substituents is manifested in broad XRD lines. The sharpening of the XRD lines is observed with increasing bismuth ions concentration in the $Eu^{3+}$ codoped $YV_{0.5}P_{0.5}O_4$ matrix. The difference in the number of the Stark components for the $^5D_0 \rightarrow {}^7F_J$ transitions indicates changes in the lattice and a number of possible $Eu^{3+}$ sites. A thorough, systematic spectroscopic analysis of $YV_{0.5}P_{0.5}O_4$: *x* mol % $Eu^{3+}$, *y* mol % $Bi^{3+}$ was conducted at room temperature and 5 K. Metal-to-metal energy transfers occurring between $Eu^{3+}$, $V^{5+}$, and $Bi^{3+}$ optically active ions have been investigated. Additionally, efficiency of the $Bi^{3+}$-$Eu^{3+}$ energy transfer (ET) was calculated.

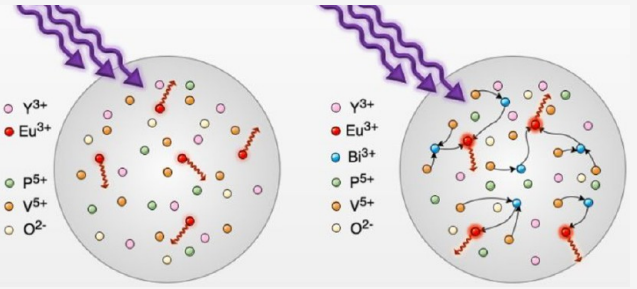


## 1. INTRODUCTION

The yttrium orthovanadate and yttrium orthophosphate matrices, doped with europium ions, are popular luminescent phosphors. This is due to their potential applications as laser host materials, polarizers, solar cells, light emitting diodes, host materials for optically active ions, etc.[1−7]

$YVO_4$ and $YPO_4$ crystallize in the zircon tetragonal system, within the space group $I4_1/amd$.[8,9] Hence, a solid-state solution of yttrium orthovanadate-phosphate can be formed.[10] Considering $YP_{0.5}V_{0.5}O_4$, its unit cell is composed of 50 mol % vanadium tetrahedral and 50 mol % phosphate tetrahedral groups, statistically substituted. Furthermore, in this work, yttrium ions in the lattice are statistically substituted with europium and bismuth ions.

In the present work, the fraction of the $YPO_4$−$YVO_4$−$BiVO_4$−$BiPO_4$ pseudoquaternary diagram (more precisely the shaded area of the $YP_{0.5}V_{0.5}O_4$−$BiVO_4$−$BiPO_4$ pseudo ternary subdiagram) is investigated (Figure 1). The bond valence sums (BVS) were obtained from VESTA,[11] and bond valence parameters were compiled in ref 12. The compounds in the shaded area have a disordered zircon-like crystal structure due to the inner structural characteristics of $YPO_4$ and $YVO_4$. Optically active europium ions are incorporated in $YP_{0.5}V_{0.5}O_4$ and $(Y,Bi)P_{0.5}V_{0.5}O_4$ for two purposes: to collect information on the local crystal structure and to investigate energy transfer processes involving $Bi^{3+}$. This paper constitutes an extension of previous reports[2,13−16] with more systematic, thorough spectroscopic analysis. Previous works[2,13,14] focus on parameters affecting the $Eu^{3+}$ emission intensity in micron-sized[14] and nanosized[2,13] systems. It was previously established that codoping $YVO_4$:$Eu^{3+}$ with $P^{5+}$, $Bi^{3+}$, and $Gd^{3+}$ greatly enhances the europium ions' emission intensity. The compositions which maximize $Eu^{3+}$ emission intensity are typically $Y_{0.9}Bi_{0.05}Eu_{0.05}$-$P_{0.5}V_{0.5}O_4$[13] or $Y_{0.45}Gd_{0.45}Bi_{0.05}Eu_{0.05}P_{0.5}V_{0.5}O_4$.[2] The reasons for this remain obscure.

Trivalent bismuth ion is known as an attractive activator in zircon vanadates.[15,17−23] Furthermore, it has been observed that $Bi^{3+}$ is an efficient luminescence sensitizer for trivalent lanthanide ions.[3,24−28] In this study bismuth and europium ions are chosen as codopants, bismuth ions improve the photoluminescence intensity of $Eu^{3+}$. This phenomenon occurs as a result of UV excitation. This is due to the CT transitions from the $Bi^{3+}$ 6s energy level to the 5d levels of the vanadate and subsequent energy transfer (ET) to $Eu^{3+}$ ions 4f orbitals.[24,29−33]

This work emphasizes characterization of the luminescent properties of these two dopants incorporated into $YV_{0.5}P_{0.5}O_4$. This matrix has a disordered structure as a result of phosphate and vanadate units being randomly dispersed throughout the lattice. This occurs because the vanadate units are ∼8% larger

Received: April 28, 2022
Published: July 28, 2022

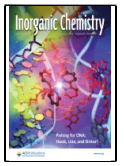

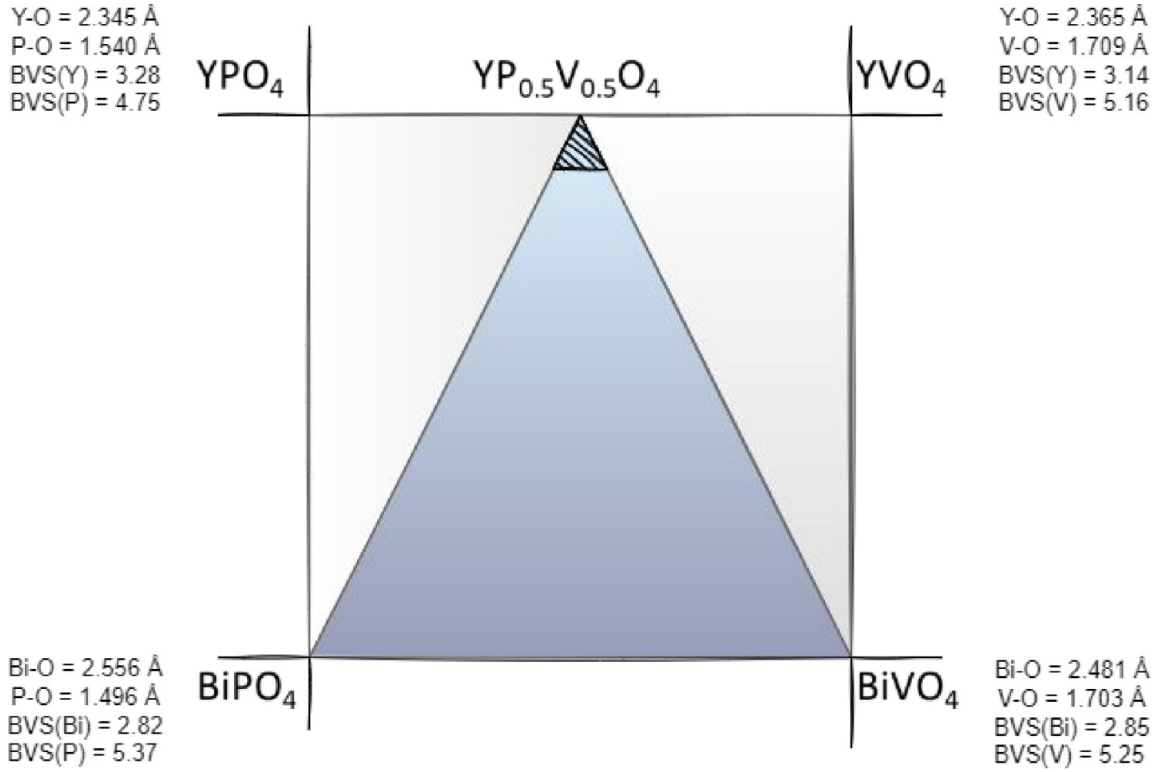


**Figure 1.** $YPO_4$–$YVO_4$–$BiVO_4$–$BiPO_4$ pseudoquaternary diagram. BVS = bond valence sum.

than the phosphates. The extent to which this disorder contributes to the efficiency of $Bi^{3+}$-$Eu^{3+}$ ET will be investigated in this work. To this end, two series of materials were synthesized. The first one was doped with varying amounts of bismuth ions, while the second was doped with varying amounts of europium ions. The chemical compositions involved doping and codoping $YV_{0.5}P_{0.5}O_4$ with $x$Bi$^{3+}$, $y$Eu$^{3+}$ where $x$ = 0, 1, 3, 5, 10, 15 mol % and $y$ = 0.5, 1, 2, 5 mol %. The solid state solutions were obtained by the wet chemistry synthesis-coprecipitation method with additional heat-treatment at 800 °C for 3 h.

## 2. EXPERIMENTAL METHODS

**2.1. Materials Synthesis.** Yttrium orthovanadate-phosphate powders, codoped with europium and bismuth ions, were obtained by the coprecipitation method. The concentrations of vanadium and phosphorus were fixed to 50 mol % each. Two series of materials were obtained: one in a function of bismuth concentration with fixed concentration of europium and vice versa. First, the concentration of europium ions was set to 1 mol %, while bismuth ion concentration changed from 0, 1, 3, 5, 10 up to 15 mol %. In the second series, the concentration of bismuth ions was set to 10 mol %, with concentrations of europium ion varying from 0.5, 1, 2, up to 5 mol %. Stoichiometric amounts of analytical grade $Y_2O_3$ (Alfa Aesar, 99.99%), $Bi_2O_3$ (Sigma-Aldrich, 99.9%), $Eu_2O_3$ (Alfa Aesar, 99.99%), $(NH_4)_2HPO_4$ (ACROS Organics, >98%) and $NH_4VO_3$ (Sigma-Aldrich, 99.5%) were used in this synthesis process.

The lanthanide and bismuth oxides were converted into nitrate salts through digestion with an excess of 65% $HNO_3$. Thereafter, the formed lanthanide and bismuth nitrates were recrystallized, and the $HNO_3$ excess was removed. Using deionized water as a solvent, separate aqueous solutions of diammonium phosphate and ammonium metavanadate were made. The vanadium and phosphorus ion sources ($NH_4VO_3$ and $(NH_4)_2HPO_4$) were mixed, followed by the nitrates ($Y(NO_3)_3$, $Bi(NO_3)_3$, $Eu(NO_3)_3$). The liquid mixture was stirred for 1.5 h at approximately 70 °C. Aqueous ammonia was used to maintain a pH of 9 during the reaction. The as-prepared precipitates were then washed and centrifuged at least three times, until neutral pH was reached. They were then dried for 24 h at 70 °C. The powders were finally crystallized by heat-treatment at 800 °C for 3 h in air.

**2.2. ICP, XRD, SEM, and TEM Analyses.** The crystal structure of synthesized materials was characterized by the X-ray Diffraction (XRD) technique using an X'Pert PRO X-ray diffractometer (Cu K$\alpha$1, 1.54060 Å) (PANalytical). Measured XRD patterns were compared to standards of $YVO_4$ (no. 78074) and $YPO_4$ (no. 79754) found in the Inorganic Crystal Structure Database (ICSD). Microstructural analyses (particle size, morphology) were performed by electron microscopy. SEM was carried out using an FEI Nova NanoSEM 230. High resolution transmission electron microscopy (HR-TEM) was performed using a Philips CM-20 Super Twin microscope. ICP-OES measurements were conducted on Thermo Scientific ICAP 7000 SERIES.

**2.3. Spectroscopic Analysis.** The Nicolet iS50 FT-IR from Thermo Scientific was used to collect infrared spectra at 300 K of samples processed in KBr pellets. The room-temperature emission spectra utilized excitation at 397, 340, and 300 nm. These spectra were collected using a FLS1000 photoluminescence spectrometer from Edinburgh Instruments. The same apparatus was used to collect the excitation spectra. The $^5D_0 \rightarrow {}^7F_2$ transition at 619 nm was monitored at room temperature for the excitation spectra measurements. Emission spectra were also recorded in response to the 266 nm excitation of a laser diode (CW) at room temperature and detected using the Hamamatsu PMA-12 photonic multichannel analyzer. The emission decay profiles were measured at 300 K using either a Ti:sapphire tunable laser or a Nd:YAG laser, a Hamamatsu R928 photomultiplier, a Jobin-Yvon THR 1000 spectrophotometer, and a digital LeCroy WaveSurfer oscilloscope. Excitation and emission spectra were collected at low temperature (5 K) using a temperature-controlled, continuous-flow liquid helium cryostat: Oxford Model CF 1204. Low temperature excitation spectra were measured with a Dongwoo Optron DM151i monochromator and a 150W ozone free lamp. The low temperature emission spectra were measured using a Dongwoo Optron DM750 monochromator, an Electro-Optical System INC PbS photodiode, or a Hamamatsu R928 photomultiplier.


https://doi.org/10.1021/acs.inorgchem.2c01465
Inorg. Chem. 2022, 61, 12237−12248

**Table 1. Elemental Composition of the Europium and Bismuth Codoped $YV_{0.5}P_{0.5}O_4$ in Molar Percentages**

| | $YV_{0.5}P_{0.5}O_4$ | | | | | | | | |
|---|---|---|---|---|---|---|---|---|---|
| element | 0.5% $Eu^{3+}$ 10% $Bi^{3+}$ | 1% $Eu^{3+}$ 10% $Bi^{3+}$ | 2% $Eu^{3+}$ 10% $Bi^{3+}$ | 5% $Eu^{3+}$ 10% $Bi^{3+}$ | 1% $Eu^{3+}$ 1% $Bi^{3+}$ | 1% $Eu^{3+}$ 3% $Bi^{3+}$ | 1% $Eu^{3+}$ 5% $Bi^{3+}$ | 1% $Eu^{3+}$ 10% $Bi^{3+}$ | 1% $Eu^{3+}$ 15% $Bi^{3+}$ |
| Y | 89.08 | 98.73 | 87.83 | 84.97 | 97.95 | 95.47 | 92.42 | 88.91 | 83.66 |
| V | 49.70 | 49.63 | 50.05 | 49.65 | 50.32 | 50.55 | 49.79 | 49.78 | 50.06 |
| P | 49.79 | 49.54 | 49.89 | 50.27 | 50.54 | 48.73 | 49.84 | 49.47 | 49.74 |
| Eu | 0.52 | 1.01 | 1.95 | 4.98 | 1.03 | 1.03 | 1.03 | 1.02 | 1.05 |
| Bi | 10.06 | | 10.01 | 10.10 | 0.96 | 3.03 | 4.97 | 9.98 | 14.94 |

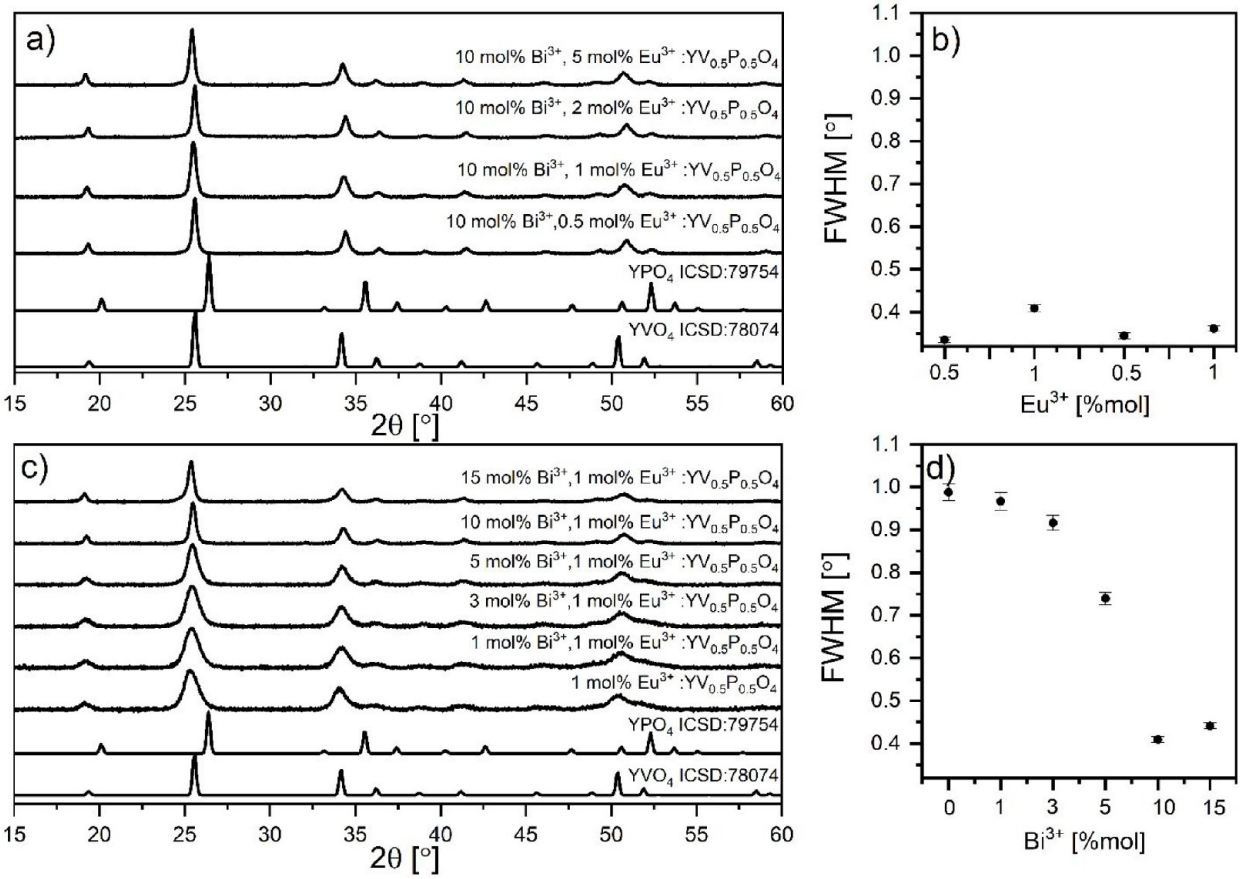


**Figure 2.** Diffractograms (a, c) and fwhm analysis (b, d) obtained for $x$ mol % $Bi^{3+}$, 1 mol % $Eu^{3+}$: $YV_{0.5}P_{0.5}O_4$ and 10 mol % $Bi^{3+}$, $y$ mol % $Eu^{3+}$: $YV_{0.5}P_{0.5}O_4$.

## 3. RESULTS AND DISCUSSION

**3.1. Structure and Morphology.** The chemical composition of all samples, analyzed by ICP-OES, is given in Table 1. It is verified that the nominal compositions are congruous with actual compositions.

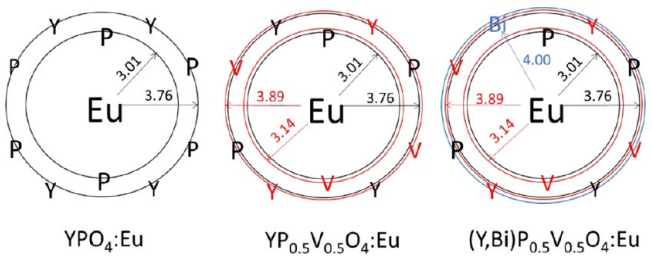


**Figure 3.** Cation coordination spheres of $Eu^{3+}$ in zircon-like $YPO_4$, $YP_{0.5}V_{0.5}O_4$, and $(Y,Bi)P_{0.5}V_{0.5}O_4$. Oxygen atoms are not represented.

XRD results confirmed the crystal phase purity of $YV_{0.5}P_{0.5}O_4$ doped derivatives (Figure 2). The XRD peaks are broadened and further confirm the structural disorder, as observed earlier.[10,12,20] This broadening originates from the size difference between $V^{5+}$ (0.36 Å, C.N. 4) and $P^{5+}$ (0.17 Å, C.N. 4), when statistically distributed in $YV_xP_{1-x}O_4$ solid solution. The lattice strains are influenced by changes in grain size. This is a result of point defects, vacancies,[34] and varying composition[35] as well as dislocations near the grain-boundaries[36] caused by the incompatibility of phosphorus and vanadium atoms. The observed changes in the fwhm of the XRD peaks may indicate the presence of lattice strains.[37]

Co-doping with $Eu^{3+}$ does not impact the lattice and, by extension, the width of the XRD peaks. In contrast, it is found that codoping with $Bi^{3+}$ contributes to narrowing of the XRD peaks (Figure 2c). This is clearly evidenced by Figure 2b,d. Additionally, increasing the $Eu^{3+}$ amount in 10 mol % $Bi^{3+}$


https://doi.org/10.1021/acs.inorgchem.2c01465
Inorg. Chem. 2022, 61, 12237−12248

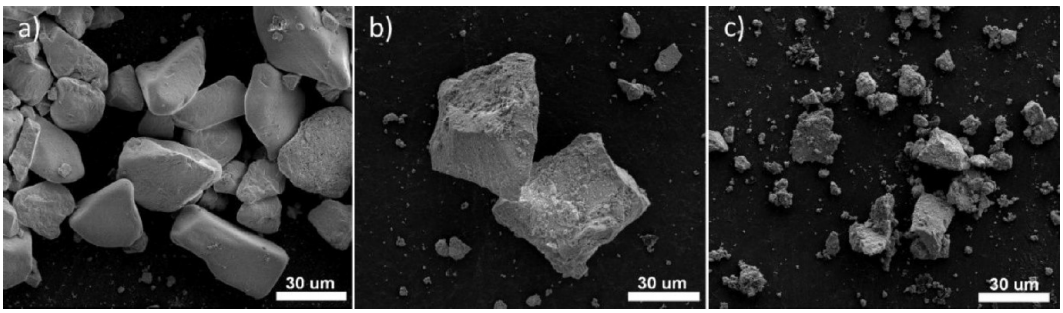


**Figure 4.** SEM images obtained for $YV_{0.5}P_{0.5}O_4$: 1 mol % $Eu^{3+}$, $xBi^{3+}$, where $x$ = 5 mol % a), 10 mol % b), and 15 mol % c).

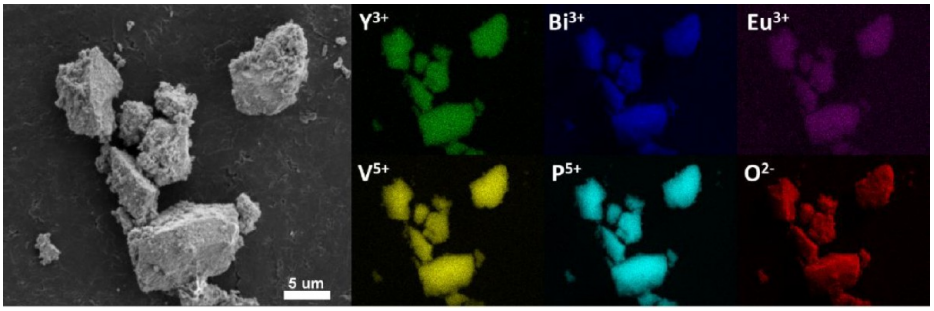


**Figure 5.** EDS maps obtained for 1 mol % $Eu^{3+}$, 10 mol % $Bi^{3+}$: $YV_{0.5}P_{0.5}O_4$.

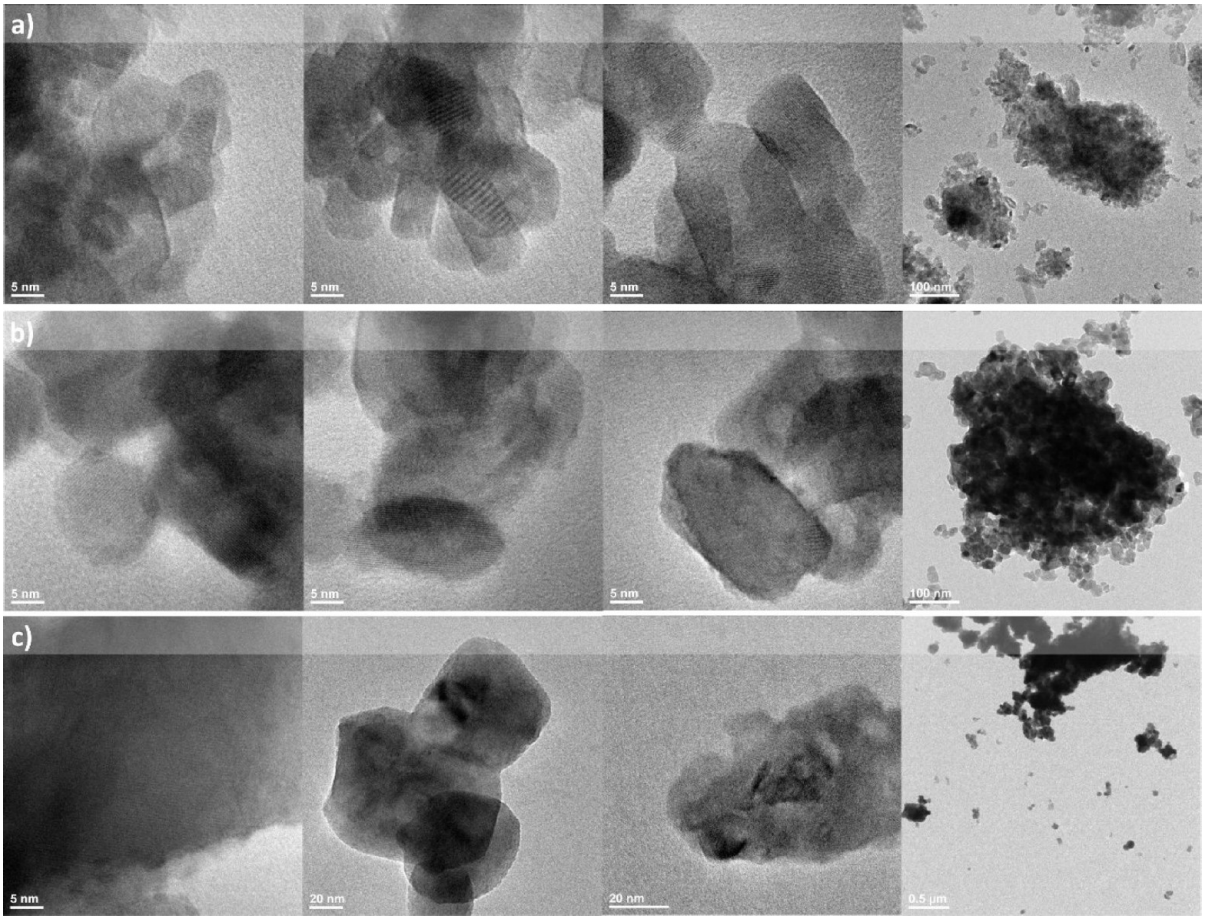


**Figure 6.** TEM images of $YV_{0.5}P_{0.5}O_4$ doped with 1 mol % $Eu^{3+}$ and 1 mol % $Bi^{3+}$ a), 1 mol % $Eu^{3+}$ and 5 mol % $Bi^{3+}$ b), and 1 mol % $Eu^{3+}$ and 15 mol % $Bi^{3+}$ (c).

codoped samples does not affect the XRD peak widths significantly.

By considering $Eu^{3+}$ as a local luminescent structural probe, we find three possible environments experienced by $Y^{3+}$ ions in



https://doi.org/10.1021/acs.inorgchem.2c01465
Inorg. Chem. 2022, 61, 12237−12248

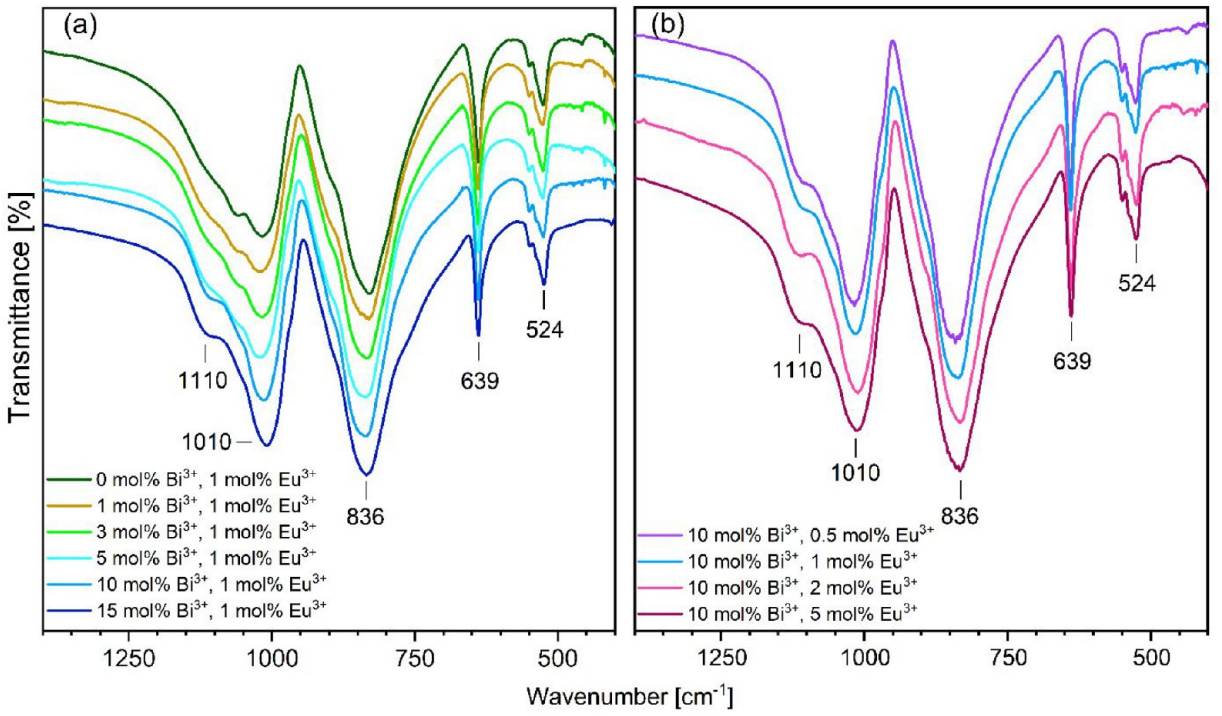


**Figure 7.** Fourier transformed infrared spectra of (a) codoped with $Bi^{3+}$ and 1 mol % $Eu^{3+}$ $YV_{0.5}P_{0.5}O_4$, with varying $Bi^{3+}$ concentrations and (b) codoped with 10 mol % $Bi^{3+}$ and $Eu^{3+}$, with varying $Eu^{3+}$ concentrations.

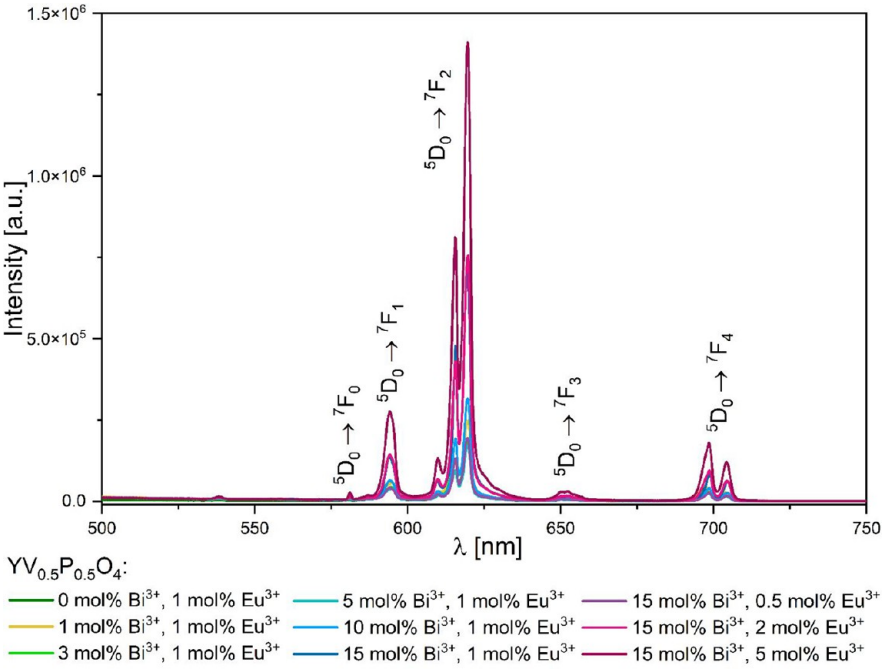


**Figure 8.** Emission spectra for *x* mol % $Bi^{3+}$, *y* mol % $Eu^{3+}$: $YV_{0.5}P_{0.5}O_4$ under 397 nm excitation at room temperature.

the compounds. This is depicted in Figure 3. In $YPO_4$, the $Eu^{3+}$ ions are surrounded by eight O atoms, thus forming a dodecahedron with $D_{2d}$ point symmetry. The first cation coordination consists of two $P^{5+}$ at 3.01 Å and respectively four $P^{5+}$ and four $Y^{3+}$ at 3.76 Å in a second coordination. The exact charge (the BVS - Bond Valence Sum) carried by these cations is given in Figure 1. Incorporation of 50% $V^{5+}$ creates two additional spheres at 3.14 and 3.89 Å (marked as red in Figure 3) with statistical occupancy. Incorporation of $Bi^{3+}$ results in a third sphere (marked as blue in Figure 3) at 4.00 Å. The probability of finding a $Bi^{3+}$ ion in this position is $P(x) = 1-(1-x)^4$ wherein *x* is the molar percentage of $Bi^{3+}$, e.g., $P(0.1) = 35\%$. The bismuth ions (1.17 Å at C.N. 8) substitute yttrium ions (1.02 Å at C.N. 8) in a statistical manner. Since $Bi^{3+}$ is about 15% larger than $Y^{3+}$, its incorporation in the crystal lattice counterbalances (at least partly) the ionic radius mismatch between $V^{5+}$ and $P^{5+}$. This inverse relationship between $V^{5+}-P^{5+}$ and $Bi^{3+}-Y^{3+}$ ionic radii mismatches reduces the lattice strains in $YV_{0.5}P_{0.5}O_4$ and thereby


https://doi.org/10.1021/acs.inorgchem.2c01465
Inorg. Chem. 2022, 61, 12237−12248

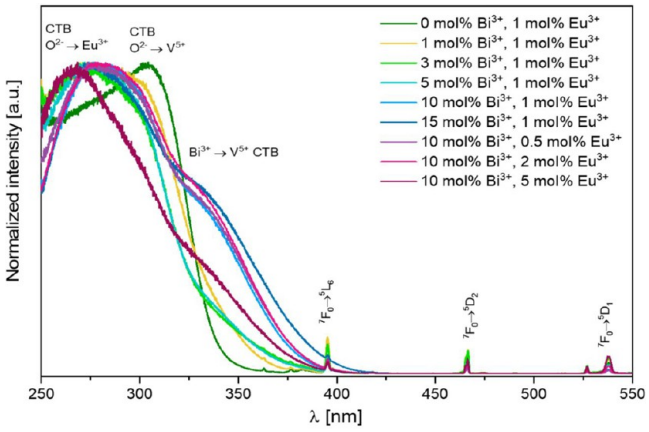


**Figure 9.** Excitation spectra for $x$ mol % $Bi^{3+}$, $y$ mol % $Eu^{3+}$: $YV_{0.5}P_{0.5}O_4$ materials measuring the intensity of the $^5D_0 \rightarrow {}^7F_2$ transition at 619 nm at room temperature.

sharpens the XRD lines as the $Bi^{3+}$ concentration is raised (Figure 2c).

SEM images of $YV_{0.5}P_{0.5}O_4$: 1 mol % $Eu^{3+}$, $x$ mol % $Bi^{3+}$ materials are depicted in Figure 4. The powders look micrometric regardless of bismuth ion concentration. As the bismuth content is raised, the particles become smaller, and their surfaces become rougher. EDS maps (Figure 5) obtained for 1 mol % $Eu^{3+}$, 10 mol % $Bi^{3+}$: $YV_{0.5}P_{0.5}O_4$ confirm random distribution of the constituents.

The TEM images in Figure 6 demonstrate that the aggregates consist in fact of nanosized particles. Analysis of the SEM (Figure 5) and TEM (Figure 6) images reveals a wide distribution of particle sizes among the samples, although we note that the particles size increases as the $Bi^{3+}$ content is raised (i.e., 19, 31, and 62 nm for doping rates of 1, 5, and 15 mol %, respectively). Differences in particles sizes contribute to the narrowing of the XRD peaks in addition to the reordering of the crystal structure. This work sheds a light into a complex structure of $Eu^{3+}$, $Bi^{3+}$: $YV_{0.5}P_{0.5}O_4$. However, to individuate or quantify the role of each effect, further crystallographic research needs to be conducted. Additionally, $d$-spacing values were calculated by the means of FFT processing in ImageJ software. d-Spacing was calculated to be $d_{101}$ = 0.45 nm for $YV_{0.5}P_{0.5}O_4$ samples codoped with 1 mol % $Eu^{3+}$ and 1 mol % $Bi^{3+}$ and 1 mol % $Eu^{3+}$ and 5 mol % $Bi^{3+}$, as well as 1 mol % $Eu^{3+}$ and 15 mol % $Bi^{3+}$. Also $d_{200}$ values were calculated. For samples codoped with 1 mol % $Eu^{3+}$ and 1 mol % $Bi^{3+}$, $d_{200}$ was 0.35 nm. However, 5 mol % and 15 mol % $Bi^{3+}$-doped samples had a $d_{200}$ value of 0.33 nm. All $d$-spacing values coincide with $d_{101}$ and $d_{200}$ values from standard patterns of $YVO_4$ ($d_{101}$ = 0.47132 nm, $d_{200}$ = 0.35591 nm) and $YPO_4$ ($d_{101}$ = 0.45379 nm, $d_{200}$ = 0.34474 nm).

**3.2. Spectroscopic Properties.** The FT-IR spectra of $YV_{0.5}P_{0.5}O_4$ codoped with $Eu^{3+}$ and $Bi^{3+}$ are shown in Figure 7. There are five strong absorption bands in the range of 1300−400 $cm^{-1}$. The peaks at 524 $cm^{-1}$ and at 639 $cm^{-1}$ represent an antisymmetric bending vibration of $\nu_4(PO_4)^{3-}$. The antisymmetric stretching vibration of $\nu_3(PO_4)^{3-}$ can be found at 1010 $cm^{-1}$ and at 1110 $cm^{-1}$.[38,39] The peak at 836 $cm^{-1}$ is ascribed to the vibration mode of the $(VO_3)^-$ group. The weak peak detected at 502 $cm^{-1}$ is related to the Y−O vibration.[40] This mode is not observed for the samples with more than 10 mol % of codopant ions concentration. The Bi−O modes are on the verge of our measurement range.[41,42]

Room temperature measurements revealed that all compounds exhibit red emission typical of $Eu^{3+}$ upon direct *4f-4f* excitation at 397 nm (Figure 8). This emission increases in intensity with increasing $Eu^{3+}$ and $Bi^{3+}$ concentrations. The highest observed emission intensity is in samples containing 10 mol % $Bi^{3+}$, 5 mol % $Eu^{3+}$: $YV_{0.5}P_{0.5}O_4$.

The excitation spectra for $x$ mol % $Bi^{3+}$, $y$ mol % $Eu^{3+}$: $YV_{0.5}P_{0.5}O_4$ materials for the $^5D_0 \rightarrow {}^7F_2$ transition at 619 nm are shown in Figure 9. Three broad transitions are observed at 266, 300, and ≈340 nm (shoulder). They correspond to the $O^{2-} \rightarrow Eu^{3+}$, $O^{2-} \rightarrow V^{5+}$, and $Bi^{3+} \rightarrow V^{5+}$ charge transfers, respectively.[2,13,14,33] The intrinsic *4f-4f* excitation lines of $Eu^{3+}$ (namely $^7F_0 \rightarrow {}^5L_6$, the $^7F_0 \rightarrow {}^5D_2$, and $^7F_0 \rightarrow {}^5D_1$ transitions) are comparatively much less intense.

Figure 10 depicts the emission spectra after excitation in the charge transfer bands. These intensities are normalized to the $^5D_0 \rightarrow {}^7F_1$ transition of $Eu^{3+}$. In addition to characteristic emission lines of $Eu^{3+}$, broad emission signals are observed. Upon 340 nm excitation, the broad signal represents the emission of the Bi−V metal-to-metal CT,[15] whereas upon 300 nm excitation, the broad signal is more surely due to perturbed vanadate groups. Upon 266 nm excitation, these bandlike emissions possibly overlap. The presence of these emission bands indicates an incomplete sensitization of $Eu^{3+}$ luminescence. Two possible sensitization paths are identified. They involve the $(VO_4)^{3-}$ units or the Bi−V self-trapped excitons as energy donors and the $Eu^{3+}$ ions as energy acceptors. Decay profiles were collected to quantify the efficiency of these energy transfers.

Decay profiles are presented in Figure 11 for 397 nm excitation (inner $^7F_0 \rightarrow {}^5L_6$ $Eu^{3+}$ transition) or 355 nm excitation (Bi−V MMCT). Corresponding average values of the luminescence lifetimes $t_{av}$, were calculated as $t_{av} = \int I(t)t\,dt / (\int I(t)\,dt)$. In this case, $I(t)$ represents the emission intensity at time $t$. These values are provided in Table 2. A plot is proposed in Figure 12 for discussion.

The parameter $\eta$ in Table 2 is related to the efficiency of the ET from $Bi^{3+}$-to-$Eu^{3+}$ in the codoped compounds. It is obtained from the equation

$$\eta = 1 - \frac{\tau_{doped}}{\tau_{undoped}}$$

where $\tau_{doped}$ is the time constant in the presence of the $Eu^{3+}$ acceptor, and $\tau_{undoped}$ is the time constant without $Eu^{3+}$ (i.e., only $Bi^{3+}$).

Figure 12(a) pertains to the inner $^7F_0 \rightarrow {}^5L_6$ excitation of $Eu^{3+}$. The left-hand side of the vertical dashed line corresponds to 1 mol % $Eu^{3+}$ doped samples with increasing $Bi^{3+}$ concentrations (compound A to compound H, excluding compound B, in Table 2). Here, an increase in emission lifetime with increasing bismuth concentration is observed up to 3 mol % $Bi^{3+}$ (compound D). These samples (A,C,D,E) also exhibit lower emission intensity relative to samples with higher $Bi^{3+}$ concentrations. This suggests a lower radiative probability from the $^5D_0$ state in these cases. Raising the $Bi^{3+}$ amount further contributes to enhance the $Eu^{3+}$ emission intensity, and it correlates with a shortening of the lifetime. This effect has already been observed in $YPO_4$:$Sm^{3+}$, $Bi^{3+}$ and is ascribed to an increased refractive index of the host lattice.[43] In this case, the radiative probability is increased, contributing to a lower emission lifetime. A synergetic effect with the reordering of the crystal structure is not excluded. This requires further


https://doi.org/10.1021/acs.inorgchem.2c01465
Inorg. Chem. 2022, 61, 12237−12248

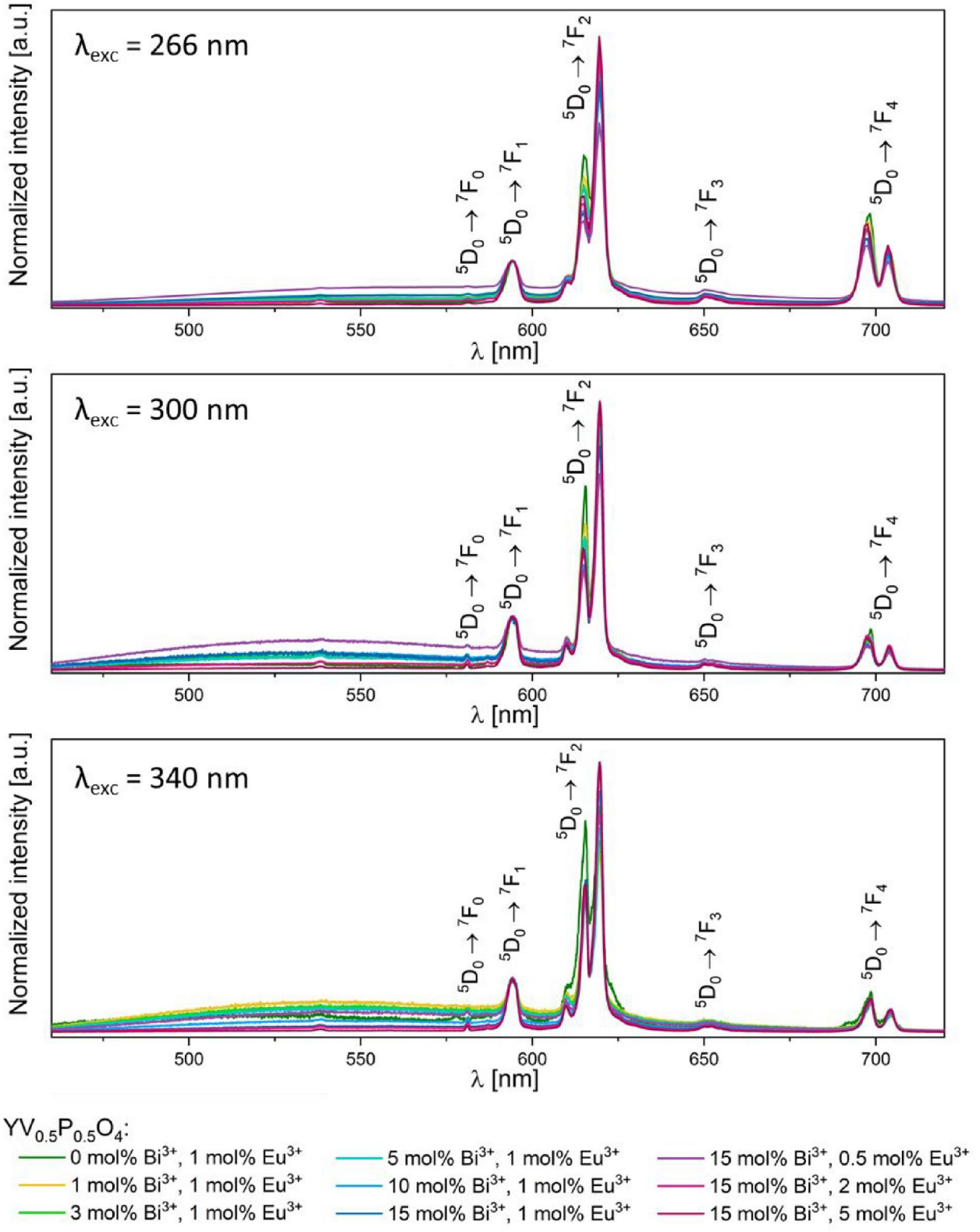


**Figure 10.** Emission spectra for *x* mol % $Bi^{3+}$, *y* mol % $Eu^{3+}$: $YV_{0.5}P_{0.5}O_4$ under 266, 300, and 340 nm excitation normalized to the $^5D_0 \rightarrow {}^7F_1$ transition of $Eu^{3+}$.

investigation. The right-hand side of the figure shows the effect of $Eu^{3+}$ content for a fixed amount of $Bi^{3+}$. In this case, the emission lifetime does not vary significantly because the medium's refractive index is unchanged. Here, the increase in emission intensity is ascribed to the larger $Eu^{3+}$ content that remains beyond the quenching concentration.[44,45]

Part (b) of Figure 12 relates to an excitation in the Bi−V MMCT band, the intensity of which exceeds by far that of the $^7F_0 \rightarrow {}^5L_6$ transition (Figure 9). In this situation, the $Eu^{3+}$


https://doi.org/10.1021/acs.inorgchem.2c01465
Inorg. Chem. 2022, 61, 12237−12248

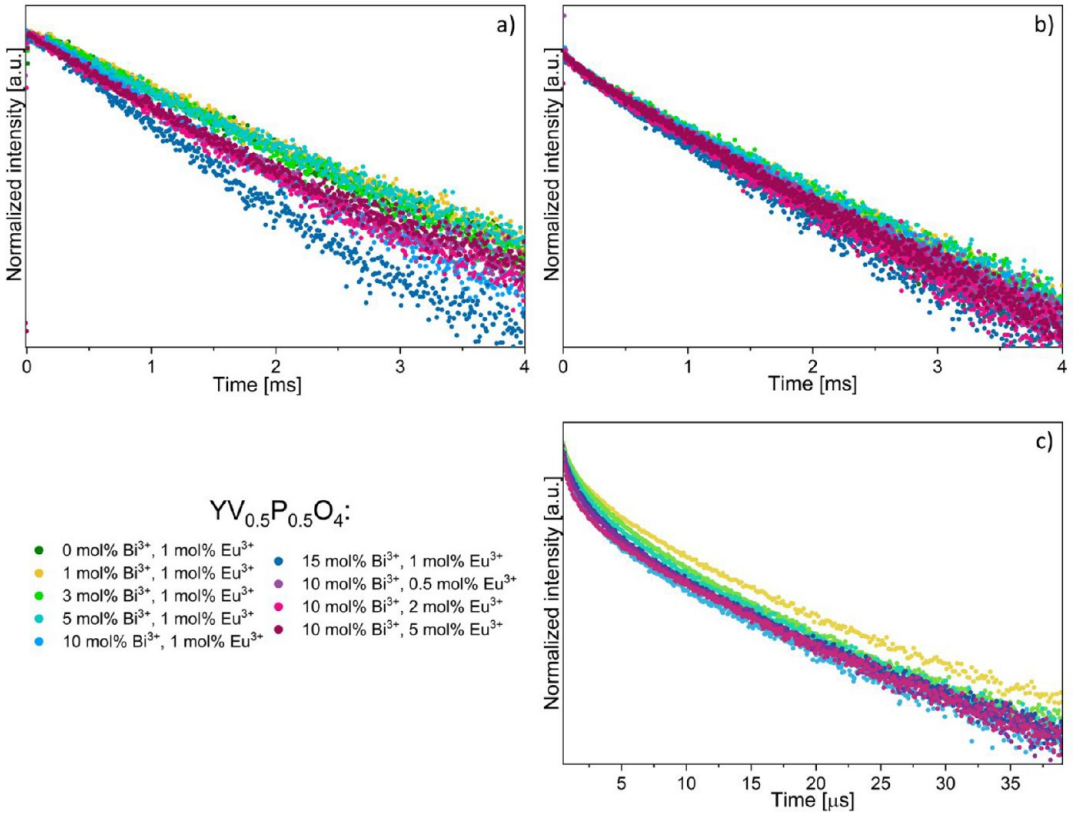


**Figure 11.** Decay time profiles measured for $^5D_0 \rightarrow {}^7F_2$ transition monitored at 619 nm $\lambda_{exc}$ = 397 nm (a), $^5D_0 \rightarrow {}^7F_2$ transition, $\lambda_{em}$ = 619 nm and $\lambda_{exc}$ = 355 nm (b), and decay profiles measured for MMCT-Bi transition $\lambda_{em}$ = 540 nm and $\lambda_{exc}$ = 355 nm (c).

**Table 2. Calculated Average Decay ($t_{av}$) and Rise ($t_{rise}$) Times for *x* mol % $Bi^{3+}$, *y* mol % $Eu^{3+}$: $YV_{0.5}P_{0.5}O_4$ Pumped with 397 and 355 nm Wavelengths**[a]

| | | $^5D_0 \rightarrow {}^7F_2$ ($Eu^{3+}$) transition at 619 nm | | Bi−V MMCT transition at 540 nm | |
|---|---|---|---|---|---|
| | | $\lambda_{exc}$ = 397 nm | $\lambda_{exc}$ = 355 nm | $\lambda_{exc}$ = 355 nm | |
| label | $YV_{0.5}P_{0.5}O_4$ | $t_{av}$ [ms] | $t_{av}$ [ms] | $t_{av}$ [μs] | $\eta$ (%) |
| A | 1 mol % $Eu^{3+}$ | 1.5 | 1.1 | | |
| B | 1 mol % $Bi^{3+}$ | | | 7.0 | |
| C | 1 mol % $Bi^{3+}$, 1 mol % $Eu^{3+}$ | 1.6 | 1.2 | 6.9 | 1.1 |
| D | 3 mol % $Bi^{3+}$, 1 mol % $Eu^{3+}$ | 1.9 | 1.2 | 5.8 | 16.5 |
| E | 5 mol % $Bi^{3+}$, 1 mol % $Eu^{3+}$ | 1.6 | 1.2 | 5.8 | 17.2 |
| F | 10 mol % $Bi^{3+}$, 1 mol % $Eu^{3+}$ | 1.3 | 1.1 | 5.5 | 20.7 |
| G | 15 mol % $Bi^{3+}$, 1 mol % $Eu^{3+}$ | 1.1 | 0.9 | 5.6 | 19.5 |
| H | 10 mol % $Bi^{3+}$, 0.5 mol % $Eu^{3+}$ | 1.1 | 1.1 | 5.7 | 17.9 |
| I | 10 mol % $Bi^{3+}$, 2 mol % $Eu^{3+}$ | 1.0 | 1.0 | 5.9 | 16.2 |
| J | 10 mol % $Bi^{3+}$, 5 mol % $Eu^{3+}$ | 1.1 | 1.0 | 6.1 | 12.9 |

[a]Each sample composition was assigned a label to facilitate the discussion below.

emission is produced after an energy transfer whose efficacy is given in Table 2. Efficacy is 20% in the $Bi^{3+}$-rich compounds F and G but tends to fall off in compounds containing more than 1% $Eu^{3+}$: $\eta$ is for instance comparable in compound D (3 mol % $Bi^{3+}$, 1 mol % $Eu^{3+}$) and in compound I (10 mol % $Bi^{3+}$, 2 mol % $Eu^{3+}$). Nevertheless, the emission intensity of compound J amounts to 6.5 times that of compound D, which demonstrates a synergy between $Bi^{3+}$ and $Eu^{3+}$ contents in $YV_{0.5}P_{0.5}O_4$. Furthermore, with respect to both 355 and 397 nm excitations, compound J exhibits the highest emission intensity related to direct $Eu^{3+}$ excitation.

At sufficiently low temperatures, vibronic interactions can be frozen out. Thus, the luminescence spectra can give more detailed information regarding the electronic transitions of $Eu^{3+}$ and can now be used as a structural probe. In 2008, Pan et. al[46] conducted investigations regarding the spectroscopic properties of $Eu^{3+}$ in $Y(V,P)O_4$ solid solution by laser-selective excitation. This work identified three symmetry sites in the yttrium orthovanadate-phosphate mixed compounds due to disorder generated by the distribution of ($PO_4$) and ($VO_4$) tetrahedra. The Judd−Ofelt intensity parameters further confirmed that significant changes in ligand polarizability contribute to differences in local environments experienced by $Eu^{3+}$.[46]

Figure 13 illustrates the excitation spectra collected at 5 K corresponding to the 619 nm emission which represents the $Eu^{3+}$ $^5D_0 \rightarrow {}^7F_2$ transition. Low temperature excitation spectra depict noticeable differences when compared to the room temperature spectra. These major differences are as follows:

(1) differences in relative intensity of the intrinsic $^7F_0 \rightarrow {}^5L_6$ transitions of $Eu^{3+}$ to the CT excitation bands in compounds containing low amounts of $Bi^{3+}$ (<5 mol %). This indicates a less efficient sensitization at 5 K. Furthermore, it demonstrates that in these conditions, the


https://doi.org/10.1021/acs.inorgchem.2c01465
Inorg. Chem. 2022, 61, 12237−12248

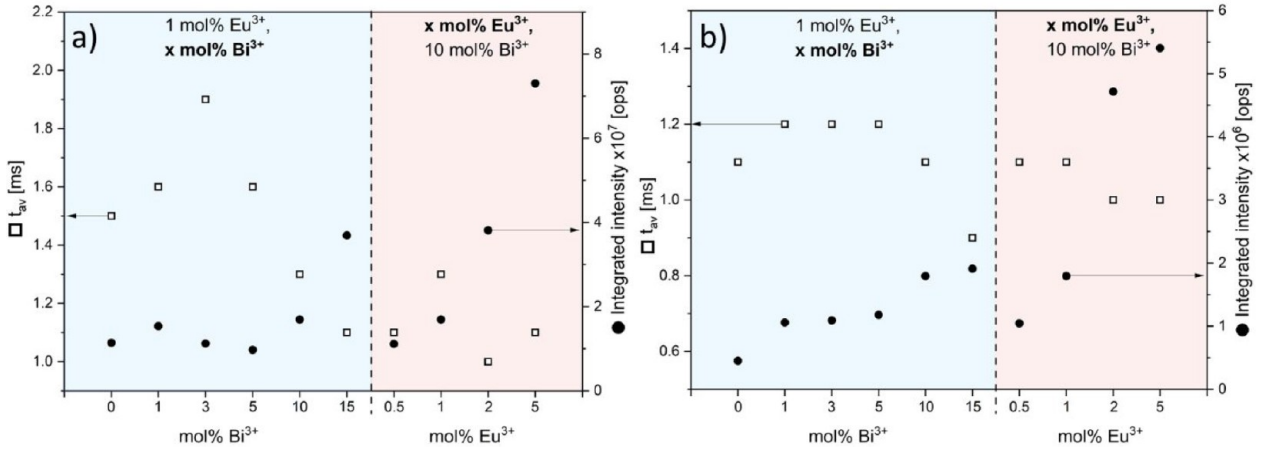


**Figure 12.** Integrated $^5D_0 \rightarrow {}^7F_2$ emission intensity (●) and average emission lifetime of $Eu^{3+}$ (□) for the different compounds listed in Table 2 in correspondence with $\lambda_{exc}$ = 397 nm (a) and $\lambda_{exc}$ = 355 nm (b).

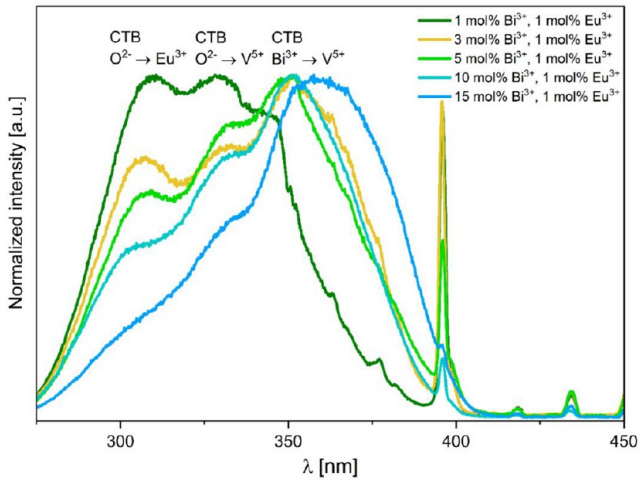


**Figure 13.** Excitation spectra for $x$ mol % $Bi^{3+}$, 1 mol % $Eu^{3+}$: $YV_{0.5}P_{0.5}O_4$ materials monitoring the 619 nm emission corresponding to the $^5D_0 \rightarrow {}^7F_2$ transition at $T$ = 5 K.

**Table 3. Stark Components (in nm) of $Eu^{3+}$ in $YVO_4$,[47] $YPO_4$,[47] and $Y_{1-x}Bi_xV_{0.5}P_{0.5}O_4$ ($x$ = 0.01, and 0.10)[b]**

| $^5D_0 \rightarrow$ | $YPO_4$ | $YVO_4$ | $Y_{0.98}Eu_{0.01}Bi_{0.01}V_{0.5}P_{0.5}O_4$ | $Y_{0.89}Eu_{0.01}Bi_{0.10}V_{0.5}P_{0.5}O_4$ |
|---|---|---|---|---|
| $^7F_0$ | 581.0 | 581.9 | | |
| $^7F_1$ | 592.7 | 593.5 | | |
| | 596.1 | 595.0 | 594.7[a] | 594.5[a] |
| $^7F_2$ | 613.4 | 615.5 | 610.5 | 609.9 |
| | 617.6 | 617.3 | 613.7 | 615.4 |
| | 619.3 | 619.4 | 615.3 | 618.8 |
| | 620.2 | 622.4 | 619.0 | 619.9 |
| | | | 619.9 | |
| $^7F_4$ | 691.6 | 690.5 | 696.7 | 698.4 |
| | 694.4 | 696.7 | 698.6 | 704.0 |
| | 696.2 | 698.5 | 703.4 | |
| | 697.3 | 699.1 | | |
| | 699.3 | 701.2 | | |
| | 703.5 | 704.5 | | |
| | 704.7 | 708.2 | | |

[a]Centroid position. [b]Data were taken at 5 K.

Bi-to-Eu energy transfer is efficiently phonon assisted. However, even at 5 K the Bi-to-Eu energy transfer regains efficacy when the $Bi^{3+}$ concentration is 10 mol %. This coincides with the increased presence of a broad excitation band which peaks at ≈360 nm and extends up to ≈400 nm, currently attributed to Bi−V MMCT.

(2) the presence of structures on the Bi−V MMCT excitation with maxima identified at ≈350, 330, and 307 nm. The relative intensity of these excitation maxima strongly depends on the $Bi^{3+}$ content in the compound. There is a notable red shift in the excitation spectra as $Bi^{3+}$ concentration increases. This shift of the Bi−V excitation edge with increasing the Bi content has been noted in previous studies, e.g., in ref32.

(3) the absence of excitation features pertaining to $O^{2-} \rightarrow Eu^{3+}$ and $O^{2-} \rightarrow V^{5+}$ charge transfers. This suggests these transitions are not involved in the sensitization process of $Eu^{3+}$ at 5 K. Therefore, only the Bi−V MMCT operates as a sensitizing channel for $Eu^{3+}$ at 5 K.

The emission spectra for 1, 3, 5, 10, 15 mol % $Bi^{3+}$, 1 mol % $Eu^{3+}$: $YV_{0.5}P_{0.5}O_4$ were collected at 5 K. These samples were excited in the CT bands and at 395 nm (Figure 14). The wavelengths of the Stark components observed in $Y_{0.98}Eu_{0.01}Bi_{0.01}V_{0.5}P_{0.5}O_4$ and $Y_{0.89}Eu_{0.01}Bi_{0.10}V_{0.5}P_{0.5}O_4$ are compiled in Table 3 and compared to reference data on $Eu^{3+}$ in $YPO_4$ and $YVO_4$.[47]

Data related to the $^5D_0 \rightarrow {}^7F_4$ transition of $Eu^{3+}$ are incomplete, when compared to the reference zircon compounds $YPO_4$:$Eu^{3+}$ and $YVO_4$:$Eu^{3+}$. The $^5D_0 \rightarrow {}^7F_1$ transitions are also poorly resolved despite the low temperature. Thereby the results are discussed based on the $^5D_0 \rightarrow {}^7F_2$ transitions. Two different signatures are noted for the $Eu^{3+}$ transitions in $Y_{0.98}Eu_{0.01}Bi_{0.01}V_{0.5}P_{0.5}O_4$ depending on the excitation wavelength. This indicates the presence of more than one $Eu^{3+}$ type site in this crystal structure, which agrees with the conclusions of Pan et al.[46] In $Y_{0.89}Eu_{0.01}Bi_{0.10}V_{0.5}P_{0.5}O_4$, however, only four Stark components (instead of five) corresponding to the $^5D_0 \rightarrow {}^7F_2$ transition were observed. The spectrum in the $^5D_0 \rightarrow {}^7F_4$ region looks also simpler. This simplification of the spectral signatures is consistent with the progressive crystal structure reordering of $YP_{0.5}V_{0.5}O_4$ concomitant with an increase in $Bi^{3+}$ concentration. This is previously observed in XRD results (Figure 2). Compared to $YPO_4$:$Eu^{3+}$ and $YVO_4$:$Eu^{3+}$, the $^5D_0 \rightarrow {}^7F_2$ spectrum of $Y_{0.89}Eu_{0.01}Bi_{0.10}V_{0.5}P_{0.5}O_4$ is more split (265 $cm^{-1}$


https://doi.org/10.1021/acs.inorgchem.2c01465
Inorg. Chem. 2022, 61, 12237−12248

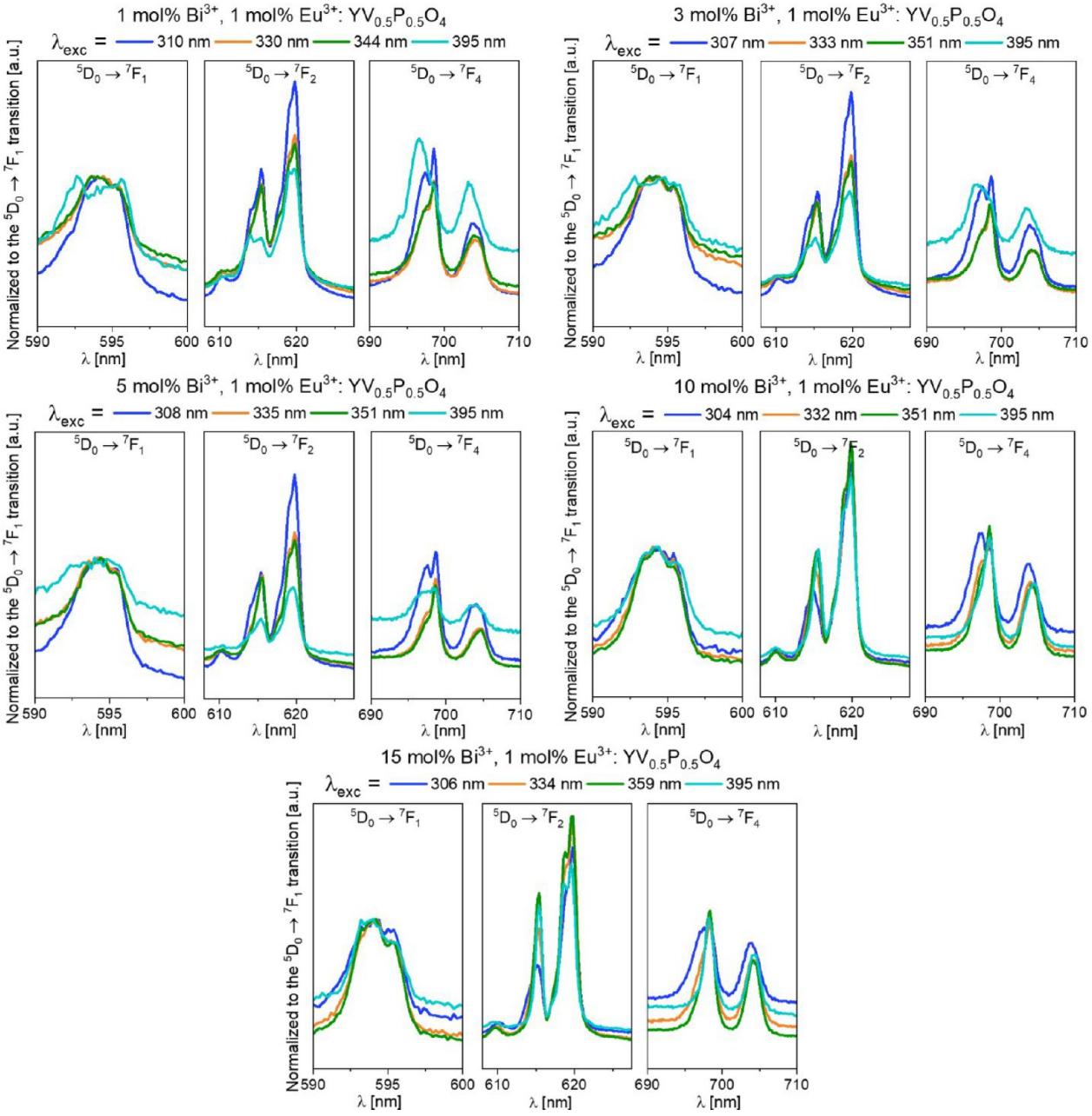


**Figure 14.** Emission spectra of 1 mol % $Eu^{3+}$ in $Y_{1-x}Bi_xV_{0.5}P_{0.5}O_4$ ($x$ = 0.01 to 0.15) upon various excitation wavelengths at 5 K. Spectra normalized to the $^5D_0 \rightarrow {}^7F_1$ transition of $Eu^{3+}$.

against 178−180 $cm^{-1}$), and its energy barycenter is upshifted. This is due to the presence of the $Bi^{3+}$ ion in the second cationic neighborhood of $Eu^{3+}$, as we have depicted in Figure 3. Owing to the BVS values given in Figure 1, it is concluded that the formal charge carried by bismuth is below that of yttrium, with the consequence that the formal charge carried by phosphorus and vanadium atoms in the Bi-doped compounds is enhanced with respect to the Bi-free compounds. This, in turn, affects the formal charge carried by the oxygen atoms in the first coordination of $Eu^{3+}$ by reinforcing the crystal field and softening the nephelauxetic effect.

## 4. CONCLUSION

The pure crystal phase of $x$ mol % $Bi^{3+}$, $y$ mol % $Eu^{3+}$: $YV_{0.5}P_{0.5}O_4$ was formed using a coprecipitation synthesis method. It is observed that codoping with $Bi^{3+}$ is followed by narrowing of the XRD peaks, but codoping with $Eu^{3+}$ does not significantly affect the widths of the peaks. The insufficient energy transfer to $Eu^{3+}$, resulting from the Bi−V MMCT and the $^3T_{1,2} \rightarrow {}^1A_1$ $(VO_4)^{3-}$ broad transition bands, is observed. Yet, $Eu^{3+}$ ion emission is enhanced by increasing $Bi^{3+}$ ion concentration. Further reaffirmed is the presence of more than one $Eu^{3+}$ site due to $(PO_4)^{3-}$ and $(VO_4)^{3-}$ substitution. Additionally, an ordering of the crystal structure of $YP_{0.5}V_{0.5}O_4$ with increasing the $Bi^{3+}$ content can be observed. It is supposed that at low temperature the sensitizing pathway of $Eu^{3+}$ is less efficient in comparison to the room temperature, and mainly the Bi−V MMCT contribution is noticeable. Based on luminescent decay times, the Bi−Eu ET efficiency was found to be the highest for bismuth-rich compounds.


https://doi.org/10.1021/acs.inorgchem.2c01465
Inorg. Chem. 2022, 61, 12237−12248

## AUTHOR INFORMATION


### Corresponding Authors

**Rafal J. Wiglusz** − *Institute of Low Temperature and Structure Research, 50-422 Wroclaw, Poland*; orcid.org/0000-0001-8458-1532; Email: r.wiglusz@intibs.pl

**Marta Wujczyk** − *Institute of Low Temperature and Structure Research, 50-422 Wroclaw, Poland*; Phone: +48 (071) 3954159/274; Email: m.wujczyk@intibs.pl; Fax: +48 (071) 3441029

### Authors

**Sara Targonska** − *Institute of Low Temperature and Structure Research, 50-422 Wroclaw, Poland*

**Philippe Boutinaud** − *Université Clermont Auvergne, Clermont Auvergne INP, CNRS, ICFC, F-63000 Clermont-Ferrand, France*

**John M. Reeks** − *Institute of Low Temperature and Structure Research, 50-422 Wroclaw, Poland*

**Adam Watras** − *Institute of Low Temperature and Structure Research, 50-422 Wroclaw, Poland*; orcid.org/0000-0003-4736-0356

Complete contact information is available at: https://pubs.acs.org/10.1021/acs.inorgchem.2c01465


### Notes

The authors declare no competing financial interest.

## ACKNOWLEDGMENTS


Regarding financial support, the authors acknowledge the National Science Centre Poland (NCN) within the project: 'Preparation and modulation of spectroscopic properties of $YXZO_4$, where X and Z − $P^{5+}$, $V^{5+}$, $As^{5+}$, doped with "$s^2$ -like" ions and codoped with rare-earth ions' (UMO-2019/33/B/ST5/02247). We express gratitude toward M. Sc. E. Bukowska for XRPD measurements and results, M. Sc. A. Hojenska for ICP measurements, PhD. D. Szymanski for measurements involving SEM-EDS, M. Sc. P. Wozniak for results and images from TEM measurements, and PhD. R. Lisiecki and PhD. B. Macalik for spectroscopic measurements at low temperature.


## REFERENCES


(1) Huang, X. Y.; Wang, J. X.; Yu, D. C.; Ye, S.; Zhang, Q. Y.; Sun, X. W. Spectral conversion for solar cell efficiency enhancement using $YVO_4$:$Bi^{3+}$, $Ln^{3+}$(Ln Dy, Er, Ho, Eu, Sm, and Yb) phosphors. *J. Appl. Phys.* **2011**, *109*, 113526.

(2) Pu, Y.; Tang, K.; Zhu, D.-C.; Han, T.; Zhao, C.; Peng, L.-L. Synthesis and Luminescence Properties of (Y, Gd)(P, V)$O_4$:$Eu^{3+}$, $Bi^{3+}$Red Nano-phosphors with Enhanced Photoluminescence by $Bi^{3+}$, $Gd^{3+}$ Doping. *Nano-Micro Lett.* **2013**, *5*, 117−123.

(3) Chen, L.; Chen, K. J.; Lin, C. C.; Chu, C. I.; Hu, S. F.; Lee, M. H.; Liu, R. S. Combinatorial approach to the development of a single mass $YVO_4$: $Bi^{3+}$,$Eu^{3+}$ Phosphor with red and green dual colors for high color rendering white light-emitting diodes. *J. Comb. Chem.* **2010**, *12*, 587−594.

(4) Wang, D.; Tie, S.; Wan, X. White light emitting from $YVO_4$/$Y_2O_3$:$Eu^{3+}$, $Bi^{3+}$ composite phosphors for UV light-emitting diodes. *Ceram. Int.* **2015**, *41*, 7766−7772.

(5) Rambabu, U.; Do Han, S. Broad band down conversion from ultra violet light to near infrared emission in $YVO_4$:$Bi^{3+}$, $Yb^{3+}$ as spectral conversion phosphor for c-Si solar cells. *Ceram. Int.* **2013**, *39*, 1603−1612.

(6) Khan, S. A.; Jalil, A.; Ullah Khan, Q.; Irfan, R. M.; Mehmood, I.; Khan, K.; Kiani, M.; Dong, B.; Khan, N. Z.; Yu, J. L.; Zhu, L.; Agathopoulos, S. New physical insight into crystal structure, luminescence and optical properties of $YPO_4$:$Dy^{3+}$\$Eu^{3+}$\$Tb^{3+}$ single-phase white-light-emitting phosphors. *J. Alloys Compd.* **2020**, *817*, 152687.

(7) Zheng, Y.; Li, F.; Wang, Y.; Zhang, K.; Peng, K. High-stability single-frequency green laser with a wedge Nd:$YVO_4$ as a polarizing beam splitter. *Opt. Commun.* **2010**, *283*, 309−312.

(8) Milligan, W. O.; Mullica, D. F. Structural Investigations of $YPO_4$, $ScPO_4$, and $LuPO_4$. *Inorganica Chem. Acta.* **1982**, *60*, 39−43.

(9) Chakoumakos, B. C.; Abraham, M. M.; Boatner, L. A. Crystal Structure Refinements of Zircon-Type $MVO_4$ (M = Sc, Y, Ce, Pr, Nd, Tb, Ho, Er, Tm, Yb, Lu). *J. Solid State Chem.* **1994**, *109*, 197−202.

(10) Wujczyk, M.; Watras, A.; Szyszka, K.; Wiglusz, R. J. Influence of vanadium concentration on up-conversion luminescence in $Er^{3+}$−$Yb^{3+}$ and $Tm^{3+}$−$Yb^{3+}$ ions pair co-doped $YV_xP_{1-x}O_4$ solid state solution. *J. Alloys Compd.* **2021**, *884*, 161022.

(11) Momma, K.; Izumi, F. An integrated three-dimensional visualization system VESTA using wxWidgets. *J. Appl. Crystallogr.* **2008**, *41*, 653−658.

(12) Brese, N. E.; O'Keeffe, M. Bond-valence parameters for solids. *Acta Crystallogr. Sect. B* **1991**, *47*, 192−197.

(13) Nguyen, H. D.; il Mho, S.; Yeo, I. H. Preparation and characterization of nanosized (Y,Bi)$VO_4$:$Eu^{3+}$ and Y(V,P)$O_4$:$Eu^{3+}$ red phosphors. *J. Lumin.* **2009**, *129*, 1754−1758.

(14) Sun, J.; Xian, J.; Xia, Z.; Du, H. Synthesis, structure and luminescence properties of Y(V,P)$O_4$:$Eu^{3+}$,$Bi^{3+}$ phosphors. *J. Lumin.* **2010**, *130*, 1818−1824.

(15) Cavalli, E.; Angiuli, F.; Mezzadri, F.; Trevisani, M.; Bettinelli, M.; Boutinaud, P.; Brik, M.G. Tunable luminescence of $Bi^{3+}$-doped $YP_XV_{1-X}O_4$($0 \le X \le 1$). *J. Phys.: Condens. Matter* **2014**, *26*, 385503.

(16) Boutinaud, P. Optical processes in (Y,Bi)$VO_4$ doped with $Eu^{3+}$ or $Pr^{3+}$. *J. Phys.: Condens. Matter* **2014**, *26*, 405501.

(17) Blasse, G.; Bril, A. Investigations on $Bi^{3+}$-Activated Phosphors. *J. Chem. Phys.* **1968**, *48*, 217−222.

(18) Boulon, G. Processus de photoluminescence dans les oxydes et les orthovanadates de terres rares polycristallins activés par l'ion $Bi^{3+}$. *J. Phys. (Paris)* **1971**, *32*, 333−347.

(19) Moncorgé, R.; Boulon, G. Investigations of the absorption and emission properties along with energy transfer in pure and $Bi^{3+}$ doped $YVO_4$. *J. Lumin.* **1979**, *18−19*, 376−380.

(20) Kang, F.; Peng, M.; Zhang, Q.; Qiu, J. Abnormal anti-quenching and controllable multi-transitions of $Bi^{3+}$ luminescence by temperature in a yellow-emitting $LuVO_4$:$Bi^{3+}$ phosphor for UV-converted white LEDs. *Chem. - A Eur. J.* **2014**, *20*, 11522−11530.

(21) Kang, F.; Sun, G.; Boutinaud, P.; Gao, F.; Wang, Z.; Lu, J.; Li, Y. Y.; Xiao, S. Tuning the $Bi^{3+}$-photoemission color over the entire visible region by manipulating secondary cations modulation in the $ScV_xP_{1-x}O_4$:$Bi^{3+}$ ($0 \le x \le 1$) solid solution. *J. Mater. Chem. C* **2019**, *7*, 9865−9877.

(22) Krasnikov, A.; Tsiumra, V.; Vasylechko, L.; Zazubovich, S.; Zhydachevskyy, Y. Photoluminescence origin in $Bi^{3+}$ - doped $YVO_4$, $LuVO_4$, and $GdVO_4$ orthovanadates. *J. Lumin.* **2019**, *212*, 52−60.

(23) Krasnikov, A.; Mihokova, E.; Nikl, M.; Zazubovich, S.; Zhydachevskyy, Y. Luminescence spectroscopy and origin of luminescence centers in bi-doped materials. *Crystals.* **2020**, *10*, 208.

(24) Chen, D.; Yu, Y.; Huang, P.; Lin, H.; Shan, Z.; Zeng, L.; Yang, A.; Wang, Y. Color-tunable luminescence for $Bi^{3+}$/$Ln^{3+}$: $YVO_4$ (Ln = Eu, Sm, Dy, Ho) nanophosphors excitable by near-ultraviolet light. *Phys. Chem. Chem. Phys.* **2010**, *12*, 7775−7778.

(25) Huang, X. Y.; Wang, J. X.; Yu, D. C.; Ye, S.; Zhang, Q. Y.; Sun, X. W. Spectral conversion for solar cell efficiency enhancement using $YVO_4$:$Bi^{3+}$,$Ln^{3+}$ (Ln Dy, Er, Ho, Eu, Sm, and Yb) phosphors. *J. Appl. Phys.* **2011**, *109*, 113526.

(26) Liu, R.; Jin, Y.; Liu, L.; Liu, Y.; Tu, D. Molten salt synthesis and color manipulation of $YVO_4$:$Bi^{3+}$,$Eu^{3+}$ phosphors. *J. Alloys Compd.* **2020**, *826*, 154187.

(27) Natarajan, V.; Dhobale, A. R.; Lu, C. H. Preparation and characterization of tunable $YVO_4$: $Bi^{3+}$, $Sm^{3+}$ phosphors. *J. Lumin.* **2009**, *129*, 290−293.

(28) Xue, J.; Wang, X.; Jeong, J. H.; Yan, X. Spectral and energy transfer in $Bi^{3+}$-$Re^{N+}$ (n = 2, 3, 4) co-doped phosphors: Extended optical applications. *Phys. Chem. Chem. Phys.* **2018**, *20*, 11516−11541.
(29) Shao, J.; Yan, J.; Li, X.; Li, S.; Hu, T. Novel fluorescent label based on $YVO_4$: $Bi^{3+}$, $Eu^{3+}$ for latent fingerprint detection. *Dye. Pigment.* **2019**, *160*, 555−562.
(30) Hara, H.; Takeshita, S.; Isobe, T.; Sawayama, T.; Niikura, S. A unique photofunction of $YVO_4$:$Bi^{3+}$,$Eu^{3+}$ nanophosphor: Photoluminescent indication for photochemical decomposition of polyurethane. *Mater. Sci. Eng. B Solid-State Mater. Adv. Technol.* **2013**, *178*, 311−315.
(31) Iso, Y.; Takeshita, S.; Isobe, T. Effects of $YVO_4$: $Bi^{3+}$, $Eu^{3+}$ Nanophosphors Spectral Down-Shifter on Properties of Monocrystalline Silicon Photovoltaic Module. *J. Electrochem. Soc.* **2012**, *159*, J72−J76.
(32) Takeshita, S.; Isobe, T.; Sawayama, T.; Niikura, S. Effects of the homogeneous $Bi^{3+}$ doping process on photoluminescence properties of $YVO_4$:$Bi^{3+}$,$Eu^{3+}$ nanophosphor. *J. Lumin.* **2009**, *129*, 1067−1072.
(33) Takeshita, S.; Isobe, T.; Sawayama, T.; Niikura, S. Low-temperature wet chemical precipitation of $YVO_4$:$Bi^{3+}$,$Eu^{3+}$ nanophosphors via citrate precursors. *Prog. Cryst. Growth Charact. Mater.* **2011**, *57*, 127−136.
(34) Qin, W.; Szpunar, J. A. Origin of lattice strain in nanocrystalline materials. *Philos. Mag. Lett.* **2005**, *85*, 649−656.
(35) Eckert, J.; Holzer, J.; Krill, C.; Johnson, W. Reversible grain size changes in ball-milled nanocrystalline Fe−Cu alloys. *J. Mater. Res.* **1992**, *7*, 1980−1983.
(36) Nazarov, A. A.; Romanov, A. E.; Valiev, R. Z. On the nature of high internal stresses in ultrafine grained materials. *Nanostructured Mater.* **1994**, *4*, 93−101.
(37) Biju, V.; Sugathan, N.; Vrinda, V.; Salini, S. L. Estimation of lattice strain in nanocrystalline silver from X-ray diffraction line broadening. *J. Mater. Sci.* **2008**, *43*, 1175−1179.
(38) Prasad, A. I.; Parchur, A. K.; Juluri, R. R.; Jadhav, N.; Pandey, B. N.; Ningthoujam, R. S.; Vatsa, R. K. Bi-functional properties of $Fe_3O_4$@$YPO_4$:Eu hybrid nanoparticles: Hyperthermia application. *Dalt. Trans.* **2013**, *42*, 4885−4896.
(39) Wu, J.; Jia, H.; Li, M.; Jia, H.; Liu, Z. Influence of pH on nanophosphor $YPO_4$:2%$Sm^{3+}$ and luminescent properties. *Appl. Phys. A Mater. Sci. Process.* **2020**, *126*, 1−8.
(40) Wu, J.; Li, M.; Jia, H.; Liu, Z.; Jia, H.; Wang, Z. Morphology formation mechanism and fluorescence properties of nano-phosphor $YPO_4$:$Sm^{3+}$ excited by near-ultraviolet light. *J. Alloys Compd.* **2020**, *821*, 153535.
(41) Chahine, A.; Et-Tabirou, M.; Pascal, J. L. FTIR and Raman spectra of the $Na_2O$-CuO-$Bi_2O_3$-$P_2O_5$ glasses. *Mater. Lett.* **2004**, *58*, 2776−2780.
(42) Boda, R.; Shareefuddin, M.; Chary, M. N.; Sayanna, R. FTIR and Optical Properties of Europium Doped Lithium Zinc Bismuth Borate Glasses. *Mater. Today Proc.* **2016**, *3*, 1914−1922.
(43) Angiuli, F.; Cavalli, E.; Boutinaud, P.; Mahiou, R. Emission properties of $Sm^{3+}$/$Bi^{3+}$-doped $YPO_4$ phosphors. *J. Lumin.* **2013**, *135*, 239−242.
(44) Yahiaoui, Z.; Hassairi, M. A.; Dammak, M. Synthesis and Optical Spectroscopy of $YPO_4$:$Eu^{3+}$ Orange−Red Phosphors. *J. Electron. Mater.* **2017**, *46*, 4765−4773.
(45) Chang, Y. S.; Huang, F. M.; Tsai, Y. Y.; Teoh, L. G. Synthesis and photoluminescent properties of $YVO_4$:$Eu^{3+}$ nano-crystal phosphor prepared by Pechini process. *J. Lumin.* **2009**, *129*, 1181−1185.
(46) Pan, G.; Song, H.; Dai, Q.; Qin, R.; Bai, X.; Dong, B.; Fan, L.; Wang, F. Microstructure and optical properties of $Eu^{3+}$ activated $YV_{1-x}P_xO_4$ phosphors. *J. Appl. Phys.* **2008**, *104*, 084910.
(47) Linares, C.; Louat, A.; Blanchard, M. Rare-Earth - Oxygen Bonding in the $LnMO_4$ Xenotime Structure: Spectroscopic Investigation and Comparative Study of Ligand Field Models. In *New Concepts*; Struct. Bond.; 1977; pp 179−207,.


https://doi.org/10.1021/acs.inorgchem.2c01465
*Inorg. Chem.* 2022, 61, 12237−12248